Salton Trough regional deformation estimated from combined trilateration and survey-mode GPS data

Greg Anderson[1], Duncan C. Agnew, and Hadley O. Johnson[2]

Cecil H. and Ida M. Green Institute of Geophysics and Planetary Physics,

University of California, San Diego

Short title: SALTON TROUGH DEFORMATION FROM TRILATERATION AND GPS

[1]Now at U.S. Geological Survey, Pasadena

[2]Now at The Prediction Company, Santa Fe, NM

Abstract. The Salton Trough in southeastern California, United States, has one of the highest seismicity and deformation rates in southern California, including 20 earthquakes M6 or larger since 1892. From 1972 through 1987, the U.S. Geological Survey (USGS) measured a 41-station trilateration network in this region. We remeasured 37 of the USGS baselines using survey-mode GPS from 1995 through 1999. We estimate the Salton Trough deformation field over a nearly 30-year period through combined analysis of baseline length time series from these two datasets. Our primary result is that strain accumulation has been steady over our observation span, at a resolution of about 0.05 μstrain/yr at 95% confidence, with no evidence for significant long-term strain transients despite the occurrence of seven large regional earthquakes during our observation period. Similar to earlier studies, we find that the regional strain field is consistent with 0.5 ± 0.03 μstrain/yr total engineering shear strain along an axis oriented $311.6 \pm 23^\circ$ east of north, approximately parallel to the strike of the major regional faults, the San Andreas and San Jacinto (all uncertainties in the text and tables are standard deviations unless otherwise noted). We also find that (1) the shear strain rate near the San Jacinto Fault is at least as high as it is near the San Andreas Fault, (2) the areal dilatation rate near the southeastern Salton Sea is significant, and (3) one station near the southeastern Salton Sea moved anomalously during the period 1987.95–1995.11.

1. Introduction

The Salton Trough is the landward extension of the Gulf of California, where the Pacific-North America plate boundary comes on land from the south (see Figure 1). About 90% of the roughly 50 mm/yr relative plate motion across the boundary is taken up on the system of large northwest-trending right-lateral strike-slip faults in the region, including the Cerro Prieto and Imperial fault (IF) zones in the south, the Elsinore and San Jacinto fault (SJF) zones to the west, and the San Andreas fault zone (SAF) on the eastern boundary [*Bennett et al.*, 1996]; as a result, this region has one of the highest strain rates in the continental United States.

The Salton Trough also has one of the highest seismicity rates in California, including at least sixteen $M \geq 6$ events and at least four $M \geq 7$ events since 1890 in an area of about 30,000 km^2. In addition, trenching along the Indio segment of the SAF shows evidence of at least four large slip events between AD 1000 and 1700, giving an average recurrence time of approximately 220 years [*Sieh*, 1986]. This segment has not ruptured since approximately AD 1685, may have since built up a slip deficit of approximately 7–8 m, and, as noted by *Bennett et al.* [1996], is thus potentially capable of a magnitude 7.5 event.

Given its unique geologic setting and high deformation and seismicity rates, the Salton Trough has been the focus of many geodetic studies, including triangulation, trilateration, leveling, and Global Positioning System (GPS) measurements [e.g., *King and Savage*, 1983; *Feigl et al.*, 1993; *Johnson et al.*, 1994; *Savage and Lisowski*, 1995;

Bennett et al., 1996]. In this paper, we describe a study of more than 25 years of trilateration and survey-mode GPS measurements of a geodetic network in the central Salton Trough. We find no evidence for long-term strain rate changes exceeding our resolution of 0.05 μstrain/yr (at 95% confidence) during our observation period. Consistent with earlier results, we also find that the spatial pattern and magnitude of strain in our study area largely match expectations from right-lateral strike-slip along the SJF and SAF, with the exception of significant regional dilatation near the southeastern Salton Sea.

2. Data Used

From 1972 through 1987, the U.S. Geological Survey made trilateration measurements [*Savage and Prescott*, 1973] of a 41-station network in the Salton Trough and surrounding mountains [*King and Savage*, 1983; *Johnson et al.*, 1994; *Savage and Lisowski*, 1995]. They surveyed this network approximately annually, with more frequent observations following significant regional earthquakes. Their final measurements were shortly after the M_w 6.6 24 Nov 1987 Superstition Hills mainshock.

From 1995 through 1999, we reoccupied 17 of the USGS stations using survey-mode GPS; Figure 2 and Table 1 give details on the subnetwork we reoccupied. Figure 3 shows the dates of our surveys and the observation duration on each day, coded by symbol as shown in the lower left corner. We used Trimble 4000 SST antennas and receivers at all stations during the 1995–98 surveys, except that we used Trimble 4000 SSE equipment at Coach, Mecca, and Orocopia in 1997. We used Ashtech Z-12 receivers

with Dorne-Margolin choke-ring antennas for the 1999 surveys at Salton and Old Beach.

We processed our GPS data using the MIT GAMIT software [*King*, 1997] to determine baseline lengths, and then combined these solutions using GLOBK to estimate baseline length time series. For the GLOBK processing, our survey-mode site coordinates were unconstrained, and we combined these with tightly-constrained coordinates for continuous GPS stations Blythe, Durmid Hill, Monument Peak, and Piñon Flat 1 from the Southern California Integrated GPS Network [*Hudnut et al.*, 2002]; we did not estimate station velocities, because we combined data from surveys close in time.

Savage and Prescott [1973] describe the techniques used in collecting and analyzing, and measurement accuracy of, the trilateration data. They show that trilateration data errors can be well-represented by

$$\sigma^2 = a^2 + b^2 L^2, \tag{1}$$

where σ^2 is the variance of the line length, a is a constant term describing the absolute precision of the technique, b is a length-proportional error term, and L is baseline length. *Johnson et al.* [1994] found the best values for a and b in southern California to be 3.8 mm and 0.16 ppm, respectively, and we use these values in our work. For the GPS data, our GAMIT/GLOBK processing returns formal estimates of the uncertainty in baseline length, but these generally underestimate the true variability in the time series, typically by a factor of 2–3 [*Anderson*, 1999]. We thus multiply the GAMIT/GLOBK formal errors by 3 to more accurately reflect the true uncertainty in our GPS data, and

use those scaled errors in our study.

3. Time series modeling

We combine the GPS and trilateration time series for each baseline (Figure 4) to determine rates of change for each baseline's length, which we will later convert to baseline strain rate. In doing so, we must account for possible systematic length biases between the trilateration and GPS data. *Savage et al.* [1996] studied length estimates from contemporaneous trilateration and GPS observations of 84 baselines in California, and found that their trilateration-estimated baseline lengths were systematically 0.283 ± 0.100 ppm longer than their GPS estimates. Accordingly, we shortened the trilateration baseline lengths by 0.283 ppm before combining them with our GPS measurements; the corrections ranged from 2.7–9.6 mm for our baseline lengths of 9.4–33.8 km.

To estimate the baseline length change rate for each combined baseline time series, we fit three model types to each series (see Table 3). For Model 1, we simultaneously estimate from the data a single rate and coseismic offsets for the 1981 Westmorland and 1987 Elmore Ranch and Superstition Hills mainshocks (with the latter two being combined into one offset because our temporal resolution does not allow us to treat them independently). For Model 2, we simultaneously estimate from the baseline series the same parameters as well as coseismic offsets for the 1979 Imperial Valley earthquake and 1992 Joshua Tree, Landers, and Big Bear events (with the 1992 events again treated as a single offset due to temporal resolution constraints). For Model 3, we compute

coseismic offsets for all these events from a priori mainshock dislocation models (see Table 2), remove these from the data, and then estimate the best-fit single rate. All our models are limited to a single rate for two reasons: (1) our temporal resolution limits our ability to resolve short-term periodic signals, and (2) if we can fit the data with only a single rate, there is no need to invoke long-term rate changes.

Applying these models systematically to all 37 baselines, we find that Model 1 can fit all but five baselines adequately at the 95% level; none of the other models fit all these 32 baselines. Figure 5a shows a typical baseline data set with the best-fit models shown as lines; residuals for these models are shown in 5b–5d, respectively. As in all figures, the error bars shown are 95% confidence; all data values and uncertainties given in the text and tables are standard deviations. In this case, all sets of residuals are compatible with zero, indicating a good fit, and all three models fit equally well.

None of our models fit at 95% confidence the five remaining baselines, which all involve ALSA and show anomalous deformation that we believe is caused by motion of ALSA between 1987.95 and 1995.11 (see Appendix B). We therefore modify Model 1 for these five baselines by allowing for an extra offset at 1995.0 to estimate the amount of anomalous motion required. Model 2 cannot be modified to fit the ALSA baselines as we have insufficient data to constrain both the JLB92 and 1995.0 offsets. Model 3 requires a priori offsets, so we apply the best-fit extra offset from Model 1 as an a priori constraint. Note that we are not suggesting that all anomalous motion occurred in a single event; by fitting the extra offset, we are only attempting to determine the total amount of anomalous motion, not how or when it occurred. Figure 6 shows the ALSA-OBCH

baseline time series and best-fit Model 1 as an example of the discrepancies observed in these data.

Model 1 alone fits all baselines at 95% confidence, with the addition of the extra offset for the ALSA baselines. In every case where Model 1 and another model fit the data acceptably, using the F-test to compare the model fits shows that Model 1 is no worse than the other model. Model 1 also has the fewest free parameters, as it only requires two offsets instead of four; we allow only two offsets in this model because the WM81 and ES87 offsets are the only coseismic offsets required by all baselines, and adding more offsets does not improve the fit significantly. We therefore prefer Model 1 and the results shown in the rest of this paper are generated from Model 1.

4. Results and Discussion

Table 4 shows for each baseline the Model 1 best-fit parameters, and Figure 7 shows the strain rates from Table 4 as a map with the network baselines coded by strain rate. We use the baseline strain rates to estimate the horizontal strain rate tensors for all four-station subnetworks in our network, averaged over the 10–30 km width of the subnetworks. We find all baselines observed between the four stations which make up each subnetwork, and combine the strain rates for those baselines using the method of *Johnson et al.* [1994] to estimate the average horizontal strain rate tensor for each subnetwork. We then compute the principal strain rates and axes for each tensor (Table 5) and decompose each tensor into the maximum right-lateral engineering shear strain rate ($\dot{\gamma}$, also called the total shear strain rate), azimuth across which the maximum is

attained ($\alpha_{\dot{\gamma}}$), and dilatation rate ($\dot{\Delta}$) for each subnetwork (Table 6 and Figure 8).

Our principal conclusion is that strain accumulation rates in the Salton Trough are very stable over time; we base this on two primary observations. First, all our baseline time series can be fit well by a model with linear strain accumulation in time punctuated by coseismic offsets. Any temporal strain transients must therefore be below our strain rate uncertainties, and a good upper bound is given by our median 95% uncertainty of 0.046 μstrain/yr. Second, our median $\dot{\gamma}$ for the Salton network as a whole (0.48 ± 0.15 μstrain/yr along an azimuth of $311.6 \pm 23^\circ$ east of north) is consistent with the average $\dot{\gamma}$ of 0.35 μstrain/yr along a 319° azimuth found by *Johnson et al.* [1994]. Our compatibility with previous analyses, even though we now span roughly twice as much time, argues for consistent strain accumulation in the Salton Trough. Further support for constant strain accumulation comes from the work of *Savage* [1995], who used principal component analysis to decompose the trilateration data and found that the Salton network data were well-explained by steady, linear strain accumulation. While we cannot rule out the possibility of strain transients with either much shorter (such as the groundwater-related signals seen by *Bawden et al.* [2001]) or much longer periods (e.g., very long-term postseismic deformation), our results indicate that during our observation span, any fluctuations in strain accumulation rate for the Salton Trough must be less than about 50 nanostrain/yr over periods from about a year to a few decades.

We also find that overall, the Salton Trough strain field is consistent with expectations in a region of primarily northwest-southeast-trending right-lateral strike-

slip faults: baselines oriented north-south show compression and east-west baselines show extension (Figure 7). Those baselines farthest from the major faults show the least strain; BEAL-SALV, COOL-PALM, ELPH-FIPK, and WILN-YAKM all show insignificant strain rates. Figure 8a shows, for each subnetwork, $\dot{\gamma}$ and $\alpha_{\dot{\gamma}}$ as bars oriented parallel to $\alpha_{\dot{\gamma}}$ and scaled by $\dot{\gamma}$ as shown in the upper left. $\dot{\gamma}$ and $\alpha_{\dot{\gamma}}$ are coherent from one subnetwork to the next, showing the redundancy in the network and indicating coherency in the regional strain field itself. Also, $\alpha_{\dot{\gamma}}$ in any given area is nearly parallel to the strike of the nearest major fault, as appropriate, and rotates smoothly from one orientation to the next. Finally, the median $\dot{\Delta}$ for the network as a whole is insignificant at 0.07 ± 0.08 μstrain/yr, with scattered subnetworks showing significant $\dot{\Delta}$; most of these subnetworks involve the station SODA, perhaps indicating inaccuracies in our corrections for damage to that station (see Appendix A).

There are two main departures from this expected picture, both of which have been observed by previous workers. As shown in Figures 8b and 8d, and as discussed in *Johnson et al.* [1994], the region near the southeastern Salton Sea is undergoing areal dilatation, at a median rate (across the five southeastern-most subnetworks) of 0.18 ± 0.04 μstrain/yr. *Johnson et al.* [1994] suggested two main models to explain this dilatation: an oblique spreading center beneath the Brawley Seismic Zone and a leaky transform connecting the Imperial and San Andreas faults through the Brawley Seismic Zone. While neither model adequately explained all the trilateration data, *Johnson et al.* [1994] preferred the oblique spreading center model.

Consistent with studies by *Johnson et al.* [1994] and *Bennett et al.* [1996], we

also find that $\dot{\gamma}$ is higher near the SJF than near the SAF; this is most easily seen as the decrease from southwest (near the SJF) to northeast (near the SAF) in the network-crossing profile of $\dot{\gamma}$ shown in Figure 8c. This strain gradient could be caused by a number of effects. First, the subnetworks near the SAF are generally larger, which might bias the average rates to lower values; however, *Johnson et al.* [1994] showed that the network geometry alone could not be responsible. Also, perhaps there is ongoing postseismic relaxation after the 1968 M6.5 Borrego Mountain earthquake, which occurred close to the west side of the Salton network. We discount this possibility since no baselines show anything but steady strain accumulation and because no earthquakes in the Salton Trough during our observation span exhibit significant postseismic transients.

If strain in the Salton Trough is primarily caused by steady slip along the SJF and SAF below some depth (the locking depth), the higher rates near the SJF imply either a shallower locking depth or a higher rate of slip for the SJF compared with the SAF. A commonly-used proxy for the locking depth is the depth of seismicity. In the polygon bounded by BLUF, PALM, COOL, SODA, FIPK, ELPH, and YAKM, 90% of the approximately 5000 earthquakes relocated by *Richards-Dinger and Shearer* [2000] occurred at depths shallower than 12 km. There are many fewer earthquakes along the southern SAF, so to define this seismicity we used a polygon consisting of OROC, COCG, a point 10 km SW of SALT, and a point 10 km W of MECC, which excludes the northernmost Brawley Seismic Zone. There are only 220 earthquakes in the catalog inside this region, and 90% of them are shallower than 8 km, implying a shallower

locking depth on the SAF.

We therefore believe that the higher strain rate is caused by a higher slip rate at depth along the SJF than along the SAF; this conclusion is somewhat controversial, but is supported by additional evidence. First, *Johnson* [1993] used extremal methods to invert trilateration data spanning the Elsinore, San Jacinto, and San Andreas faults for self-consistent bounds on slip rates along those faults and showed that the SJF and SAF slip rate bounds were 7–25 and 11–23 mm/yr, respectively, allowing a faster SJF slip rate. It is important to note, however, that the block model analysis by *Bennett et al.* [1996] of survey-mode GPS data in this region gives slip rates of 26 ± 2 and 9 ± 2 mm/yr on the SAF and SJF, respectively. Recent geologic work also supports comparable or higher slip rates along the SJF relative to the SAF. *Rockwell et al.* [1990] found a slip rate of 6–23 mm/yr (preferred range: 12–13 mm/yr) along the Anza segment of the SJF, while work by *Brown* [1990] gives an estimate of 10–17 mm/yr, and *Kendrick et al.* [2002] argue for ≥ 20 mm/yr along the northern SJF. *Dorsey* [2003] has improved the *Keller et al.* [1982] alluvial fan offset measurements and gives a new SAF slip rate estimate of 15 ± 3 mm/yr, which is in good agreement with the 6–12 mm/yr rate determined by *Sieh and Williams* [1990] near Salt Creek. A reasonable range of geologic slip rate estimates is thus 15–20 mm/yr for the SJF and about 15 mm/yr for the SAF, and the *Johnson* [1993] work allows for a faster SJF, so it is at least plausible that the current slip rate at depth along the SJF is comparable to or faster than that along the SAF. A more definitive result may be possible from a future analysis of all the data (trilateration and independent GPS) collected in this region, and in the process of

being assembled by the Southern California Earthquake Center.

5. Conclusions

We have combined trilateration and survey-mode GPS observations of a 17-station network in the Salton Trough to study deformation of that region. We find that our data are fit well by linear strain accumulation, punctuated by coseismic offsets at the times of the 1981 Westmorland and 1987 Elmore Ranch and Superstition Hills mainshocks. There is no evidence for significant long-term strain transients at a resolution of about 0.05 μstrain/yr, even though seven significant regional earthquakes occurred during our observation span. The overall strain field is well-represented by about 0.5 ± 0.03 μstrain/yr of total engineering shear strain along an orientation $311.6 \pm 23^\circ$ east of north, approximately parallel to the strike of the San Andreas and San Jacinto faults, the major faults crossed by our network.

We also find that the shear strain rate near the San Jacinto fault is at least as high as that along the San Andreas Fault, which we believe is caused by a higher slip rate at depth along the San Jacinto fault. Perhaps due to a spreading center or leaky transform fault beneath the Brawley Seismic Zone, we find 0.18 ± 0.04 μstrain/yr of areal dilatation near the southeastern Salton Sea. Finally, ALSA, a station located near the southeastern Salton Sea, moved anomalously 35.6 ± 8.1 mm to the WSW during the period 1987.95–1995.11, most likely in response to nearby geothermal power production.

Appendix A: Disturbed Benchmarks

Two of the marks we reoccupied had changed significantly between the time of the last trilateration observation and our GPS surveys. Bluff No. 1 1939 (bluff_rm1 for trilateration measurements; our code BLUF), the site used for trilateration measurements, was damaged. Our GPS observations were at the mark SDGPS 09 RM 1 (SD91) set by San Diego County in 1991 in an existing piece of concrete. We made GPS ties in 1997 between the original mark BLFO and the azimuth mark BLFA, and between SD91 and its main mark SD09. In 1995 the U.S. Geological Survey made a GPS tie between BLFA and SD09. Combining all these, we get a horizontal distance of 28.444 m from BLFO to SD91 (total distance 28.477 m) in azimuth 10.79°. The NGS taped distance from BLFO to BLUF was 28.466 m in azimuth 10.80°. SD91 was clearly set in the BLUF monument; field examination suggests that SD91 was in the same horizontal location as BLUF to within a few mm.

SODA was set in a 10-cm-diameter concrete-filled iron pipe which projected about 20 cm above the ground, which we found broken at ground level when we originally reoccupied the site in 1997; we therefore observed at Soda No. 2 1939 (SOD2). On 1997:252, we reset SODA's broken pipe to its original position and simultaneously observed at SODA and SOD2 to make an eccentric correction from SOD2 to SODA. We compared the original SODA-SOD2 horizontal distance and azimuth from the NGS datasheet for SODA to our GPS-derived values, and find no significant difference, but given the residual dilatation for subnetworks involving SODA (seen in Figure 8c), we

may have small errors in our eccentric corrections due to uncorrected deformation of SODA's pipe.

Appendix B: Anomalous Motion of ALSA

None of our models fit at 95% confidence the combined trilateration/GPS data for the five baselines to ALSA (ALSA-COCG, ALSA-OBCH, ALSA-SALT, ALSA-SALV, and ALSA-SODA). Since none of the other measurements into COCG, OBCH, SALT, SALV, and SODA show any departure from steady motion, we believe that the explanation is movement of ALSA between 1987.95 and 1995.11.

If the north and east components of ALSA's anomalous displacement are Δ_N and Δ_E, then the change in length d_i of the i-th baseline is

$$d_i = \Delta_N \cos(\alpha_i) + \Delta_E \sin(\alpha_i), i = 1, 2, \ldots, N, \tag{B1}$$

where α_i is the azimuth for baseline i. Using this equation and the observed offsets on the five ALSA baselines, we find a least-squares best-fit motion of ALSA of 35.6 ± 8.1 mm along an azimuth of $253.8 \pm 9.5°$; we show this motion and the individual baseline vector offsets in Figure B1a. Figure B1b shows the expected offset from Equation B1 as a function of azimuth (solid line with 95% confidence limits), which matches the observed offsets (shown as circles) well, supporting our assumption that ALSA moved anomalously. Additionally, we compared GPS ties between ALSA and its three nearby reference marks (RMs, see Table 1) to measurements made when the RMs were set, and we conclude that ALSA has remained stable (at ≤ 5 mm) relative to the RMs,

indicating that a larger area than ALSA alone moved anomalously.

We believe this motion reflects deformation caused by nearby geothermal power production. Production at the Salton Sea geothermal field began in 1982, and in 1990 was increased by a factor of 20; also, the production wells are located within 4 km of ALSA, and to its south and southwest. The timing of production and expected direction of surface motion due to subsidence from it are consistent with ALSA's anomalous motion.

Acknowledgments. Our field work would have been impossible without the efforts and skill of Wade Blackard, Steve Bralla, Stephen Dockter, and Don Elliott, and we thank them for their help. We thank Landells Aviation, particular our pilot Steve, for flying us to mountaintop survey points which would have been difficult if not impossible to reach otherwise (including some we would have bet you couldn't land on). Master Chief Horner with Naval Special Weapons Group 1 and Gunnery Sergeant Andrew Fenwick at Marine Corps Air Station Yuma were very helpful in arranging access to sites Coach, Beals, and Salvation, which are located in the Chocolate Mountains Aerial Gunnery Range. We used trilateration data collected by the USGS Crustal Strain Group, and we thank them for their efforts and for making the data available to us. We acknowledge the Southern California Integrated GPS Network and its sponsors, the W.M. Keck Foundation, NASA, NSF, USGS, SCEC, for providing data used in this study. We created our figures using the Generic Mapping Tools [*Wessel and Smith*, 1991, 1998], and we thank Pål Wessel, Walter Smith, and all the others who have contributed to that software suite. This work makes use of event locations computed using waveforms recorded by the Southern California Seismic Network (SCSN), which is

operated jointly by the Seismological Laboratory at Caltech and the U.S. Geological Survey, Pasadena. We thank Ken Hudnut and Nancy King for thoughtful reviews of this manuscript and many fruitful discussions of the work in progress. This research was supported by NSF grant EAR-96286744 and U.S. Geological Survey NEHRP grant 1434-HQ-97-GR-02979. This research was supported by the Southern California Earthquake Center. SCEC is funded by NSF Cooperative Agreement EAR-0106924 and USGS Cooperative Agreement 02HQAG0008. The SCEC contribution number for this paper is 730.

References

Anderson, G. J., I. Studies in crustal deformation using GPS and tiltmeters; II. New statistical techniques in static stress triggering, Ph.D. thesis, University of California, San Diego, La Jolla, Calif., 1999.

Bawden, G. W., W. Thatcher, R. S. Stein, K. W. Hudnut, and G. Peltzer, Tectonic contraction across Los Angeles after removal of groundwater pumping effects, *Nature*, *412*, 812–815, 2001.

Bennett, R. A., R. E. Reilinger, W. Rodi, Y. Li, and M. N. Toksöz, Coseismic fault slip associated with the 1992 M_w 6.1 Joshua Tree, California, earthquake: Implications for the Joshua Tree-Landers earthquake sequence, *J. Geophys. Res.*, *100*, 6443–6461, 1995.

Bennett, R. A., W. Rodi, and R. E. Reilinger, Global Positioning System constraints on fault slip rates in southern California and northern Baja, Mexico, *J. Geophys. Res.*, *101*, 21,943–21,960, 1996.

Brown, R. D., Quaternary deformation, in *The San Andreas Fault System, California: U.S. Geol. Surv. Prof. Pap., 1515*, edited by R. E. Wallace, pp. 83–113, United States Geological Survey, 1990.

Dorsey, R. J., Late Pleistocene slip rate on the Coachella Valley segment of the San Andreas fault and implications for regional slip partitioning, paper presented at 99th Annual Meeting, Cordilleran Section, Geological Society of America, Puerto Vallarta, Mexico, 1 April 2003.

Feigl, K. L., D. C. Agnew, Y. Bock, D. Dong, A. Donnellan, B. H. Hager, T. A. Herring, D. D. Jackson, T. H. Jordan, R. W. King, S. Larsen, K. M. Larson, M. M. Murray, Z.-K.

Shen, and F. H. Webb, Space geodetic measurements of crustal deformation in central and southern California, 1984–1992, *J. Geophys. Res.*, *98*, 21,677–21,712, 1993.

Hartzell, S. H., and T. H. Heaton, Inversion of strong ground motion and teleseismic waveform data for the fault rupture history of the 1979 Imperial Valley, California, earthquake, *Bull. Seismol. Soc. Am.*, *73*, 1553–1583, 1983.

Hauksson, E., Crustal structure and seismicity distribution adjacent to the Pacific and North America plate boundary in southern California, *J. Geophys. Res.*, *105*, 13,875–13,903, 2000.

Hudnut, K. W., Y. Bock, J. E. Galetzka, F. H. Webb, and W. H. Young, The Southern California Integrated GPS Network SCIGN, in *Seismotectonics in Convergent Plate Boundary*, edited by Y. Fujinawa and A. Yoshida, pp. 167–190, Terrapub, Tokyo, 2002.

Johnson, H. O., Techniques and studies in crustal deformation, Ph.D. thesis, University of California, San Diego, 1993.

Johnson, H. O., D. C. Agnew, and F. K. Wyatt, Present-day crustal deformation in southern California, *J. Geophys. Res.*, *99*, 23,951–23,974, 1994.

Keller, E. A., M. S. Bonkowski, R. J. Korsh, and R. J. Shlemon, Tectonic geomorphology of the San Andreas fault zone in the southern Indio Hills, Coachella Valley, California, *Geol. Soc. Am. Bull.*, *93*, 46–56, 1982.

Kendrick, K. J., D. M. Morton, S. Wells, and R. W. Simpson, Spatial and temporal deformation along the northern San Jacinto fault, southern California: Implications for slip rates, *Bull. Seismol. Soc. Am.*, *92*, 2782–2802, 2002.

King, N. E., and J. C. Savage, Strain-rate profile across the Elsinore, San Jacinto, and San

Andreas faults near Palm Springs, California, 1973–81, *Geophys. Res. Lett.*, *10*, 55–57, 1983.

King, R. W., *Documentation for the GAMIT GPS Analysis Software*, Department of Earth, Atmospheric, and Planetary Sciences, MIT, 1997.

Larsen, S., R. Reilinger, H. Neugebauer, and W. Strange, Global Positioning System measurements of deformation associated with the 1987 Superstition Hills earthquake: Evidence for conjugate faulting, *J. Geophys. Res.*, *97*, 4885–4902, 1992.

Richards-Dinger, K. B., and P. M. Shearer, Earthquakes in southern California obtained using source-specific station terms, *J. Geophys. Res.*, *105*, 10,939–10,960, 2000.

Rockwell, T. K., C. C. Loughman, and P. M. Merrifield, Late Quaternary rate of slip along the San Jacinto fault zone near Anza, southern California, *J. Geophys. Res.*, *95*, 8593–8605, 1990.

Savage, J. C., Principal component analysis of interseismic deformation in southern California, *J. Geophys. Res.*, *100*, 12,703–12,718, 1995.

Savage, J. C., and M. Lisowski, Interseismic deformation along the San Andreas fault in southern California, *J. Geophys. Res.*, *100*, 12,703–12,717, 1995.

Savage, J. C., and W. H. Prescott, Precision of Geodolite distance measurements for determining fault movements, *J. Geophys. Res.*, *78*, 6001–6008, 1973.

Savage, J. C., M. Lisowski, and W. H. Prescott, Observed discrepancy between Geodolite and GPS distance measurements, *J. Geophys. Res.*, *101*, 25,547–25,552, 1996.

Sieh, K., Slip rate across the San Andreas fault and prehistoric earthquakes at Indio, California, *EOS Trans. AGU*, *67*, 1200, 1986.

Sieh, K. E., and P. L. Williams, Behavior of the southernmost San Andreas fault during the past 300 years, *J. Geophys. Res.*, *95*, 6629–6645, 1990.

Wald, D. J., and T. H. Heaton, Spatial and temporal distribution of slip for the 1992 Landers, California, earthquake, *Bull. Seismol. Soc. Am.*, *84*, 668–691, 1994.

Wessel, P., and W. H. F. Smith, Free software helps map and display data, *EOS Trans. AGU*, *72*, 441, 445–446, 1991.

Wessel, P., and W. H. F. Smith, New, improved version of Generic Mapping Tools released, *EOS Trans. AGU*, *79*, 579, 1998.

Greg Anderson, U.S. Geological Survey, 525 South Wilson Avenue, Pasadena CA 91106-3212 (ganderson@usgs.gov); Duncan C. Agnew, Cecil H. and Ida M. Green Institute of Geophysics and Planetary Physics, University of California, San Diego, La Jolla CA 92093-0225; Hadley O. Johnson, The Prediction Company, 236 Montezuma Avenue, Santa Fe, NM 87501

Received _____

Publication draft for *Bulletin of the Seismological Society of America*, 15 July 2003

This manuscript was prepared with AGU's LaTeX macros v5, with the extension package 'AGU^{++}' by P. W. Daly, version 1.6b from 1999/08/19.

Figure Captions

Figure 1. Regional setting of the Salton Trough, California. Light solid lines indicate major regional faults and dots show background seismicity ($M > 2.5$, 1981–2002) from the catalog of *Hauksson* [2000] and the TriNet catalog. Mainshock focal mechanisms for the M_w 6.6 1979 Imperial Valley (IV79) and M_w 6.1 1992 Joshua Tree (JT92), M_w 7.3 1992 Landers (LN92), and M_w 6.5 1992 Big Bear (BB92) events are shown by the beach balls; heavy lines represent the fault planes used for dislocation modeling of coseismic offsets (see text). Heavy dashed box shows region used in Figure 2. Dotted line shows the United States/Mexico border, and San Diego, Palm Springs, and Brawley are shown for reference.

Figure 2. Subset of USGS Salton trilateration network reoccupied using survey-mode GPS. Beach balls indicate the mainshock focal mechanisms for the M_w 5.7 1981 Westmorland (WM81), M_w 6.2 1987 Elmore Ranch (ER87), and M_w 6.6 1987 Superstition Hills (SH87) earthquakes and are plotted at the mainshock epicenters. Thin solid lines show San Andreas fault (SAF), San Jacinto fault zone (SJFZ), Elsinore fault (EF), and Imperial fault (IF). Heavy solid lines represent the fault planes used for dislocation modeling of coseismic offsets (see text), and Brawley is shown for reference.

Figure 3. Dates and durations of GPS observations at each station. Circles indicate 0–6 hour observation durations, squares 6–12 hours, inverted triangles 12–18 hours, and triangles 18–24 hours. Observation dates are 1995:041, 1995:042, 1996:095, 1997:211, 1997:211, 1997:252, 1997:253, 1997:297, 1998:037, 1998:038, 1998:043, 1999:048, and 1999:049 (year:day of year).

Figure 4. Salton Trough time series. Filled symbols represent data within three standard deviations from Model 1 expected data. Open symbols are outliers greater than 3 standard deviations from the Model 1 predictions. Vertical scale is in mm; time series have been offset arbitrarily for visibility.

Figure 5. (a) Length time series and Model 1–3 fits for SALT-SODA baseline. Data are shown as filled circles with 95% confidence regions. Models 1, 2, and 3 fits are shown by the solid, dotted, and dashed lines, respectively. Note that all models fit the data well, and that the rates and offsets fit are approximately similar across all models. Times of the IV79, WM81, ES87, and JLB92 offsets are marked by the vertical dotted lines. (b–d) Residuals (in mm) for Models 1–3, shown as filled circles with 95% confidence regions; note that all residuals are compatible with zero misfit (zero shown as horizontal dotted line for reference).

Figure 6. (a) Length time series and model fits for ALSA-OBCH baseline. Lines and circles are as in Figure 5. Note the additional offset at 1995.0 to account for anomalous motion of ALSA; in this case, the discrepancy between the expected value from trilateration and observed GPS measurement is 37.7 ± 6.8 mm. Note that, with the addition of this offset, Model 1 fits the data well, while Model 3 does not. (b–c) Residuals (in mm) for Models 1 and 3, as in Figure 5. Note that all residuals are compatible with zero misfit once the additional offset is added.

Figure 7. Baseline strain rates for Model 1. Baselines which are stretching are solid, while contracting lines are dashed; line thickness varies with strain rate as shown in upper right, with values in μstrain/yr. ALSA is marked by an empty triangle to emphasize that the ALSA baselines have an additional offset. Dotted lines represent baselines with insignificant (at 95% confidence) strain rates. Note expected pattern of N-S compression and E-W extension.

Figure 8. (a) $\dot{\gamma}$ and $\alpha_{\dot{\gamma}}$ for each unique four-station subnetwork, using the Model 1 principal strain rates. Bars are plotted at the centroid of each subnetwork with significant $\dot{\gamma}$, scale with $\dot{\gamma}$ as shown in the upper left, and are oriented parallel to $\alpha_{\dot{\gamma}}$. (b) $\dot{\Delta}$ for only those subnetworks with significant $\dot{\Delta}$. Open circles: $\dot{\Delta} > 0$; solid circles: $\dot{\Delta} < 0$. Circles scale with $\dot{\Delta}$ as shown in upper left. (c) Cross-network profile of $\dot{\gamma}$ (with 95% confidence regions) along the line A–A' in (a). Bands labeled "SJFZ" and "SAF" refer to the San Jacinto Fault Zone and San Andreas Fault, respectively. The SJFZ band is wider because the SJFZ has multiple fault strands through our network, while the SAF is relatively simple. (d) Profile of dilatation rates. Note high $\dot{\Delta}$ in southeastern part of network.

Figure B1. (a) Black vectors with thin arrowheads show the observed offsets in the ALSA baselines. Thin lines show 95% confidence limits on the observed offsets. Heavy arrow with wide head and 95% confidence limit shows best-fit motion of ALSA. (b) Solid line with dotted lines representing 95% confidence intervals shows baseline offsets expected due to ALSA best-fit motion. Circles with 95% confidence bars are observed offsets for Alamo baselines; these are fit well by the best-fit model.

Tables

Table 1. Salton Network Survey-Mode GPS Stations

Station Code	N. Lat. (°)	E. Lon. (°)	Ell. Elev. (m)	NGS PID	Stamping
ALSA	33.19636	-115.61117	-73.365	DW1398	ALAMO 1934
ALM3	33.19617	-115.61123	-73.873	-	ALAMO NO 3 1966
ALM4	33.19638	-115.61131	-73.913	-	ALAMO NO 4 1966
ALM5	33.19650	-115.61117	-73.939	-	ALAMO NO 5 1978
BEAL	33.35462	-115.35830	748.051	DW1389	BEALS
BLFA	33.25827	-116.23326	348.790	DX4904	BLUFF 1939 (az. mark)
BLFO	33.25674	-116.23311	359.757	DX4902	brass rod [Bluff]
COCG	33.44525	-115.65613	659.151	-	COACH 1972
COOL	33.38227	-116.07724	650.012	DX4890	COOLIDGE 1939
ELPH	33.04511	-116.17549	1001.952	-	ELEPHANT 1978
FIPK	32.98178	-115.98077	677.563	DB1601	FISH 1939
MECC	33.63424	-116.02960	467.766	DX4840	MECCA HILL 1931
OBCH	33.27903	-115.50114	-16.025	DW1393	unstamped disk [Old Beach]
OBC1	33.27925	-115.50123	-16.132	-	OLD BEACH NO 1 1934
OBC2	33.27906	-115.50099	-15.984	-	OLD BEACH NO 2 1934
OBC3	33.28218	-115.49523	-9.994	-	OLD BEACH NO 3 1934
OROC	33.56907	-115.77980	1129.930	DW1485	OROCOPIA 1931

Table 1. (continued)

Station Code	N. Lat. (°)	E. Lon. (°)	Ell. Elev. (m)	NGS PID	Stamping
OTLL	33.13119	-116.10905	105.377	DX4908	OCOTILLO 1939 1974
PALM	33.30786	-116.12618	788.851	DX4903	PALM 1939
SALT	33.43096	-115.81564	-3.506	DW1461	SALTON
SALV	33.23365	-115.26148	596.129	DW1379	SALVATION
SD09	33.25686	-116.23317	358.982	-	SDGPS 9 1992
SD91[a]	33.25700	-116.23305	358.404	-	SDGPS 9 RM1 1992
SOD2	33.17853	-115.91791	30.389	DW1460	unstamped disk [Soda]
SODA[b]	33.17860	-115.91788	31.659	-	SODA NO 2 1939
WILN	33.17729	-116.43372	1365.501	DX4934	WILSON 1939
YAKM	33.10238	-116.27750	1081.273	DX4920	YAK 1939

[a]Station is reset of trilateration mark Bluff RM 1; we use BLUF as the ID for both the trilateration and GPS stations (see Appendix A).

[b]Station damaged before GPS survey; we made GPS observations at SOD2 and made an eccentric correction to SODA (see Appendix A).

Coordinates in WGS-84

Table 2. Significant Regional Earthquakes, 1972–1999

Date	Name	M_w	N. Lat.	E. Lon.	Code	Model Source
15 Oct 1979	Imperial Valley	6.6	32.61	-115.32	IV79	*Hartzell and Heaton* [1983]
26 Apr 1981	Westmorland	5.7	33.11	-115.63	WM81	*Savage and Lisowski* [1995]
24 Nov 1987	Elmore Ranch	6.2	39.09	-115.79	ER87	*Larsen et al.* [1992]
24 Nov 1987	Superstition Hills	6.6	33.01	-115.85	SH87	*Larsen et al.* [1992]
23 Apr 1992	Joshua Tree	6.1	33.96	-116.32	JT92	*Bennett et al.* [1995]
28 Jun 1992	Landers	7.3	34.20	-116.44	LN92	*Wald and Heaton* [1994]
28 Jun 1992	Big Bear	6.5	34.20	-116.83	BB92	*Wald and Heaton* [1994]

We combine the ER87 and SH87 offsets into one offset (ES87) and JT92, LN92, and BB92 into one offset (JLB92) because our temporal sampling does not allow us to resolve individual offsets.

Table 3. Model Characteristics

Model	IV79	WM81	ES87	JLB92	1995.0
1	-	Fitted	Fitted	-	Fitted
2	Fitted	Fitted	Fitted	Fitted	-
3	A priori	A priori	A priori	A priori	A priori*

*Model 1 value imposed as a priori constraint

All models have single rate and intercept in addition to specified offsets. 1995.0 offset applies only to ALSA baselines and accounts for anomalous motion of ALSA (see Appendix B). Fitted offsets are estimated from data, a priori using dislocation models in Table 2.

Table 4. Model 1 Baseline Results

Site 1	Site 2	Rate[a] mm/yr	WM81[b] mm	ES87[c] mm	1995.0[d] mm	Strain Rate[e] 10^{-8}/yr
ALSA	COCG	2.5 ± 0.8	25.6 ± 5.7	1.1 ± 7.3	-1.4 ± 9.8	8.9 ± 2.8
ALSA	OBCH	1.6 ± 0.5	25.6 ± 4.0	-2.2 ± 5.3	37.7 ± 6.8	11.7 ± 3.6
ALSA	SALT	5.7 ± 0.6	16.8 ± 5.4	18.7 ± 7.5	-13.0 ± 8.6	17.5 ± 1.8
ALSA	SALV	4.1 ± 0.8	21.1 ± 6.6	-2.3 ± 7.9	35.1 ± 11.0	12.4 ± 2.3
ALSA	SODA	7.3 ± 0.7	-7.9 ± 5.6	14.6 ± 7.2	-22.9 ± 10.6	25.5 ± 2.3
BEAL	COCG	2.4 ± 0.7	0.4 ± 5.7	5.1 ± 8.2	—	8.1 ± 2.3
BEAL	OBCH	1.0 ± 0.5	2.8 ± 4.3	3.4 ± 5.4	—	6.4 ± 2.9
BEAL	SALV	0.4 ± 0.6	2.0 ± 4.6	0.5 ± 6.2	—	2.6 ± 3.7
BLUF	ELPH	-3.6 ± 0.6	-8.1 ± 4.6	-6.6 ± 7.4	—	-14.8 ± 2.3
BLUF	OTLL	-4.0 ± 0.6	4.4 ± 4.7	21.5 ± 9.4	—	-22.1 ± 3.2
BLUF	PALM	3.0 ± 0.5	-11.4 ± 3.6	-12.7 ± 5.6	—	26.5 ± 3.9
BLUF	SODA	7.2 ± 1.1	-12.0 ± 7.4	20.1 ± 16.8	—	23.5 ± 3.7
BLUF	WILN	2.9 ± 0.9	-8.8 ± 6.0	4.5 ± 13.0	—	14.1 ± 4.4
COCG	OBCH	2.4 ± 0.4	-2.7 ± 4.6	1.2 ± 6.1	—	10.4 ± 1.8
COCG	OROC	1.5 ± 0.5	-1.1 ± 4.0	-0.7 ± 6.4	—	8.2 ± 2.6
COCG	SALT	2.5 ± 0.4	-0.9 ± 3.8	2.8 ± 5.2	—	16.4 ± 2.4
COOL	MECC	-5.7 ± 0.5	7.4 ± 4.9	-0.5 ± 6.8	—	-20.3 ± 1.7

Table 4. (continued)

Site 1	Site 2	Rate[a] mm/yr	WM81[b] mm	ES87[c] mm	1995.0[d] mm	Strain Rate[e] 10^{-8}/yr
COOL	OTLL	-6.2 ± 0.5	-1.7 ± 4.9	-5.8 ± 6.8	—	-22.2 ± 1.7
COOL	PALM	-0.4 ± 0.4	0.3 ± 3.5	1.3 ± 5.5	—	-4.1 ± 4.5
COOL	SALT	4.6 ± 0.4	-8.2 ± 4.6	5.2 ± 6.2	—	18.6 ± 1.7
COOL	SODA	-1.9 ± 0.6	-11.7 ± 5.2	51.8 ± 6.8	—	-7.1 ± 2.0
ELPH	FIPK	0.6 ± 0.5	-6.1 ± 4.1	-69.2 ± 6.7	—	3.2 ± 2.5
ELPH	OTLL	1.3 ± 0.5	-12.2 ± 3.6	6.2 ± 5.7	—	11.3 ± 3.9
FIPK	OTLL	-1.7 ± 0.4	-13.4 ± 4.2	-41.7 ± 5.8	—	-8.4 ± 2.0
FIPK	SODA	-5.5 ± 0.5	1.9 ± 4.8	-6.9 ± 6.1	—	-24.4 ± 2.2
MECC	OROC	4.3 ± 0.5	-1.8 ± 4.5	0.2 ± 6.6	—	17.7 ± 1.9
MECC	SALT	1.2 ± 0.5	4.0 ± 5.2	13.1 ± 7.1	—	4.1 ± 1.6
OBCH	SALT	6.7 ± 0.5	4.5 ± 5.6	-1.7 ± 7.5	—	19.9 ± 1.4
OBCH	SALV	1.1 ± 0.5	11.6 ± 4.9	4.2 ± 6.2	—	5.0 ± 2.0
OROC	SALT	-2.9 ± 0.4	-2.2 ± 3.9	12.8 ± 5.3	—	-18.5 ± 2.3
OTLL	PALM	-5.1 ± 0.5	-7.9 ± 4.1	-8.0 ± 6.6	—	-26.0 ± 2.5
OTLL	SODA	6.0 ± 0.5	-14.4 ± 4.4	6.3 ± 5.7	—	32.0 ± 2.4
OTLL	WILN	5.1 ± 0.6	-18.3 ± 5.6	-24.8 ± 8.2	—	16.6 ± 1.9

Table 4. (continued)

Site 1	Site 2	Rate[a] mm/yr	WM81[b] mm	ES87[c] mm	1995.0[d] mm	Strain Rate[e] 10^{-8}/yr
OTLL	YAKM	2.8 ± 0.4	-10.6 ± 4.2	1.9 ± 5.5	—	17.1 ± 2.4
PALM	SODA	1.7 ± 0.7	-16.4 ± 5.0	30.5 ± 7.2	—	7.1 ± 2.8
SALT	SODA	-7.0 ± 0.6	1.4 ± 5.5	28.4 ± 7.2	—	-23.5 ± 1.9
WILN	YAKM	0.4 ± 0.5	0.1 ± 4.0	-5.6 ± 6.2	—	2.4 ± 2.7

[a]Rate of change of baseline length

[b]1981 Westmorland earthquake coseismic offset

[c]1987 Elmore Ranch/Superstition Hills combined coseismic offset

[d]Additional offset for ALSA discrepancy

[e]Baseline linear strain rate, extension positive

Positive rates and offsets indicate that a particular baseline is lengthening. For ALSA baselines, a positive offset indicates ALSA moved away from the other station.

Figures

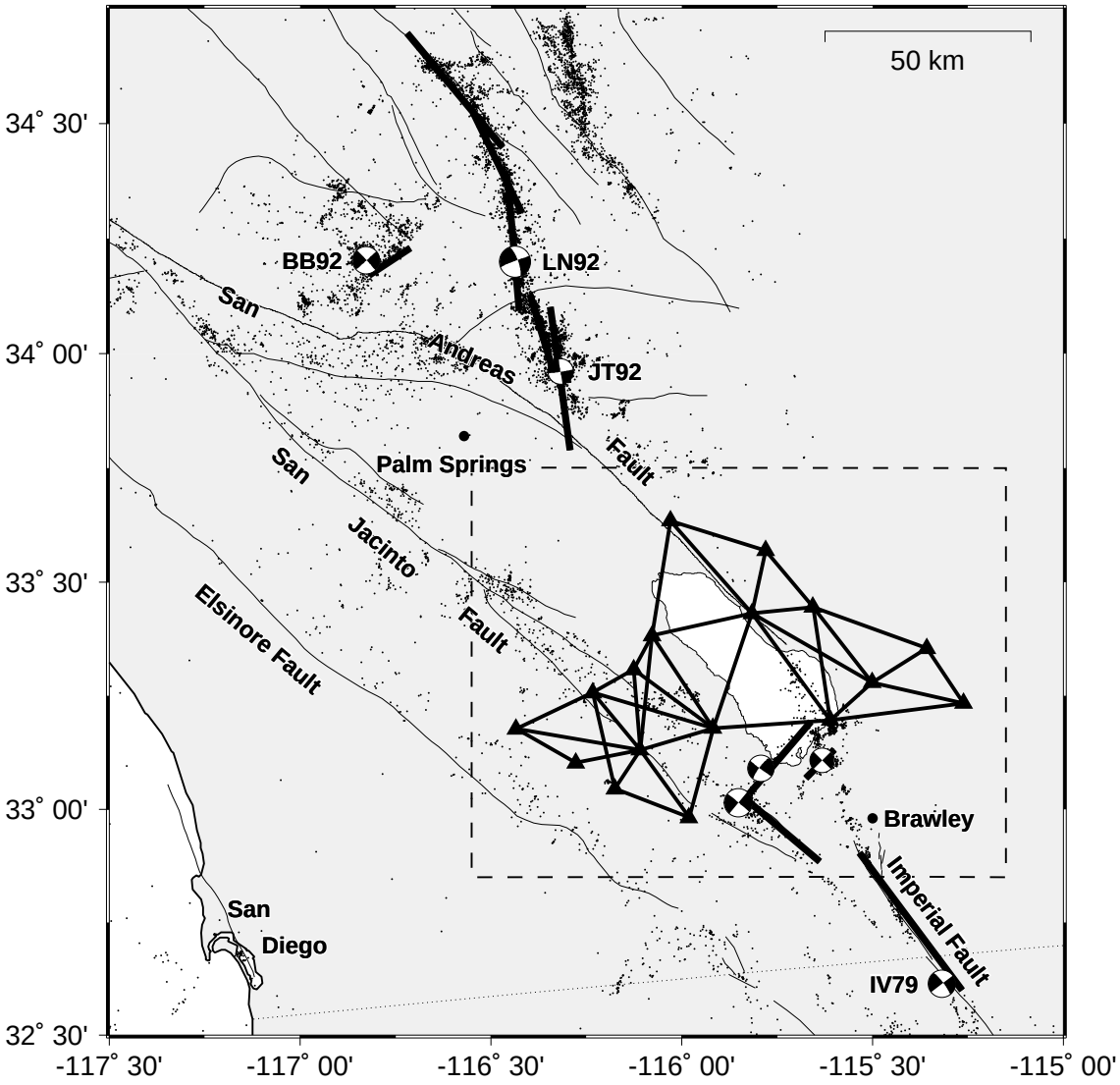

Figure 1. Regional setting of the Salton Trough, California. Light solid lines indicate major regional faults and dots show background seismicity ($M > 2.5$, 1981–2002) from the catalog of *Hauksson* [2000] and the TriNet catalog. Mainshock focal mechanisms for the M_w 6.6 1979 Imperial Valley (IV79) and M_w 6.1 1992 Joshua Tree (JT92), M_w 7.3 1992 Landers (LN92), and M_w 6.5 1992 Big Bear (BB92) events are shown by the beach balls; heavy lines represent the fault planes used for dislocation modeling of coseismic offsets (see text). Heavy dashed box shows region used in Figure 2. Dotted line shows the United States/Mexico border, and San Diego, Palm Springs, and Brawley are shown for reference.

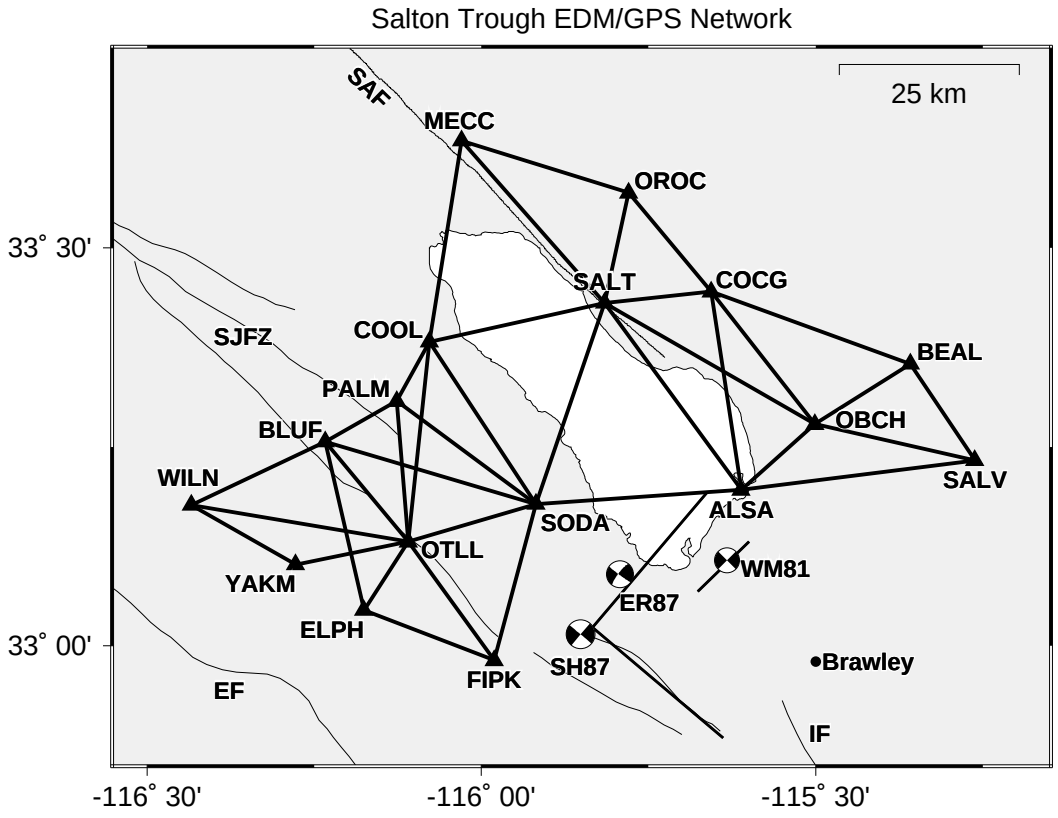

Figure 2. Subset of USGS Salton trilateration network reoccupied using survey-mode GPS. Beach balls indicate the mainshock focal mechanisms for the M_w 5.7 1981 Westmorland (WM81), M_w 6.2 1987 Elmore Ranch (ER87), and M_w 6.6 1987 Superstition Hills (SH87) earthquakes and are plotted at the mainshock epicenters. Thin solid lines show San Andreas fault (SAF), San Jacinto fault zone (SJFZ), Elsinore fault (EF), and Imperial fault (IF). Heavy solid lines represent the fault planes used for dislocation modeling of coseismic offsets (see text), and Brawley is shown for reference.

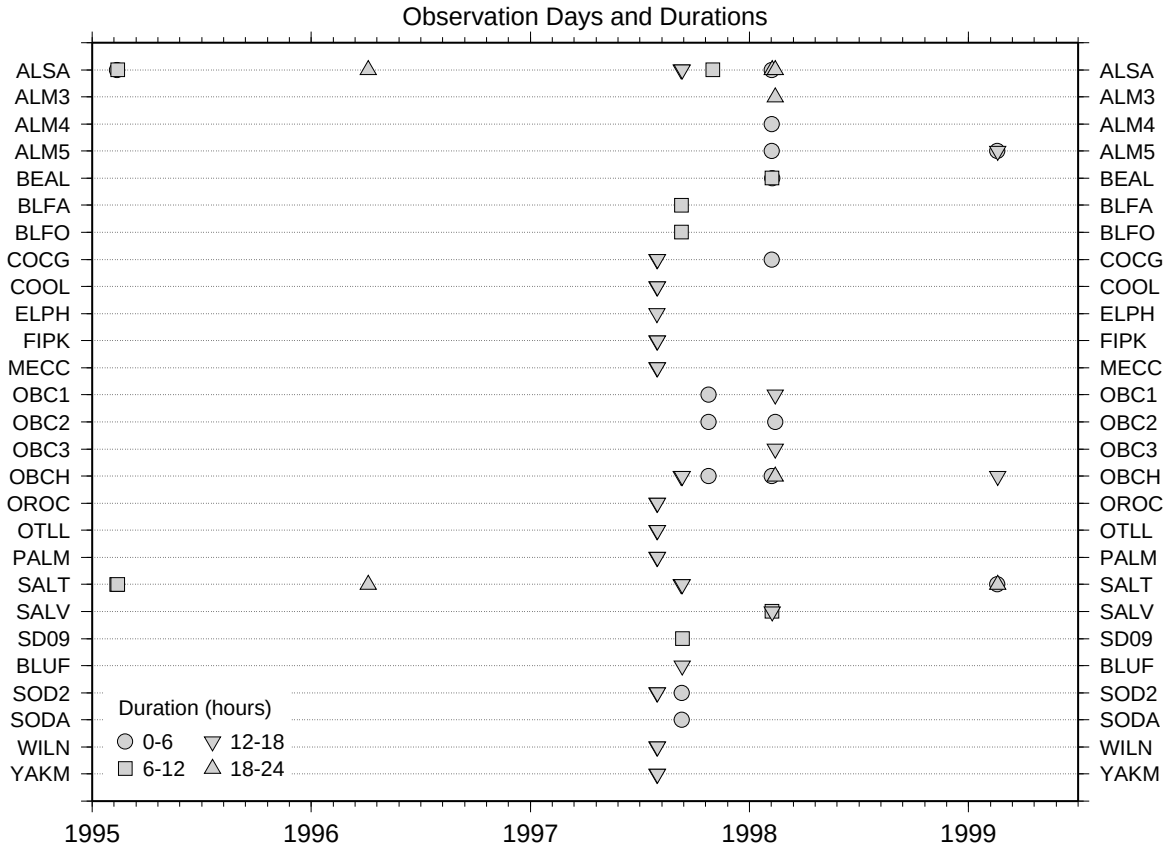

Figure 3. Dates and durations of GPS observations at each station. Circles indicate 0–6 hour observation durations, squares 6–12 hours, inverted triangles 12–18 hours, and triangles 18–24 hours. Observation dates are 1995:041, 1995:042, 1996:095, 1997:211, 1997:211, 1997:252, 1997:253, 1997:297, 1998:037, 1998:038, 1998:043, 1999:048, and 1999:049 (year:day of year).

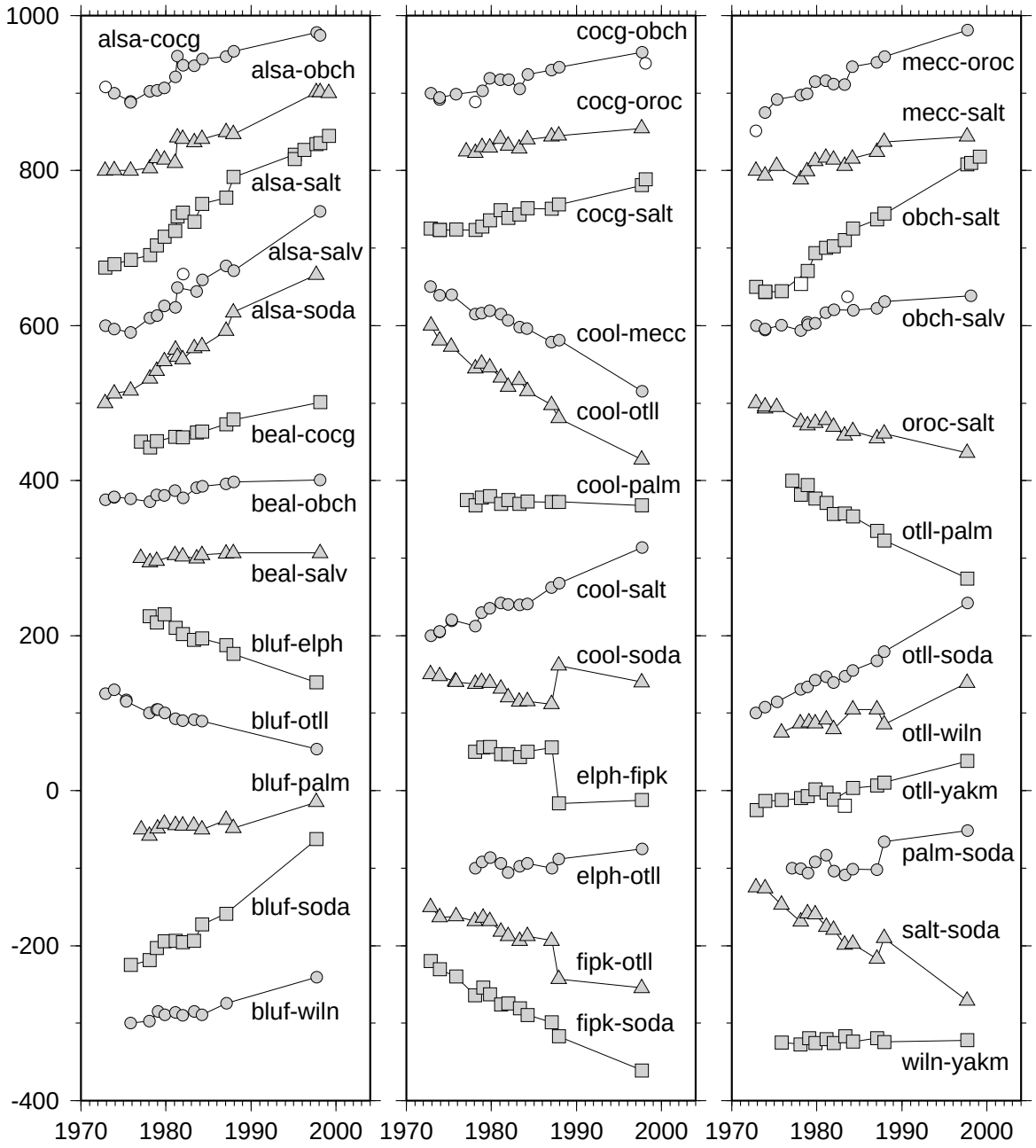

Figure 4. Salton Trough time series. Filled symbols represent data within three standard deviations from Model 1 expected data. Open symbols are outliers greater than 3 standard deviations from the Model 1 predictions. Vertical scale is in mm; time series have been offset arbitrarily for visibility.

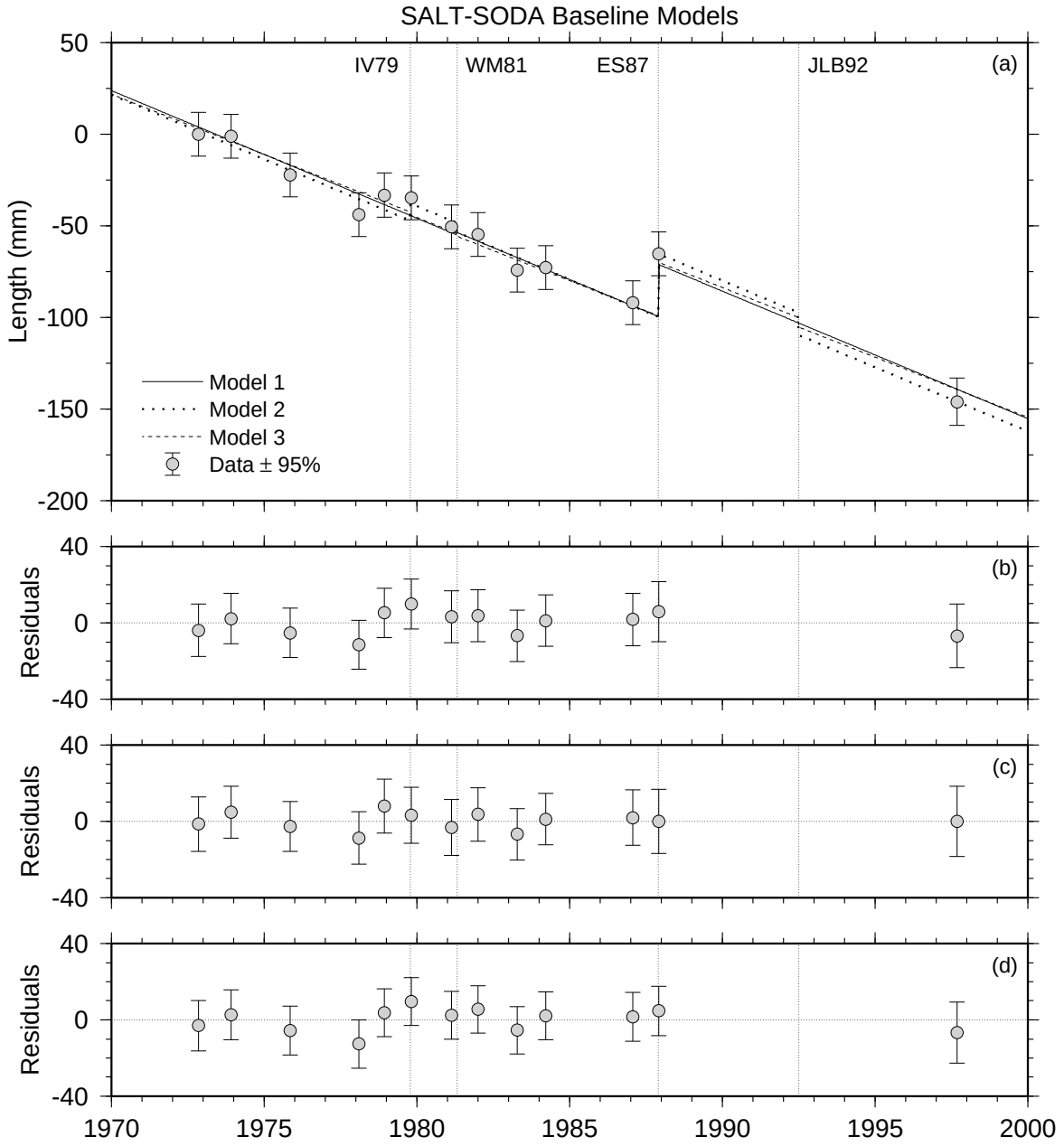

Figure 5. (a) Length time series and Model 1–3 fits for SALT-SODA baseline. Data are shown as filled circles with 95% confidence regions. Models 1, 2, and 3 fits are shown by the solid, dotted, and dashed lines, respectively. Note that all models fit the data well, and that the rates and offsets fit are approximately similar across all models. Times of the IV79, WM81, ES87, and JLB92 offsets are marked by the vertical dotted lines. (b–d) Residuals (in mm) for Models 1–3, shown as filled circles with 95% confidence regions; note that all residuals are compatible with zero misfit (zero shown as horizontal dotted line for reference).

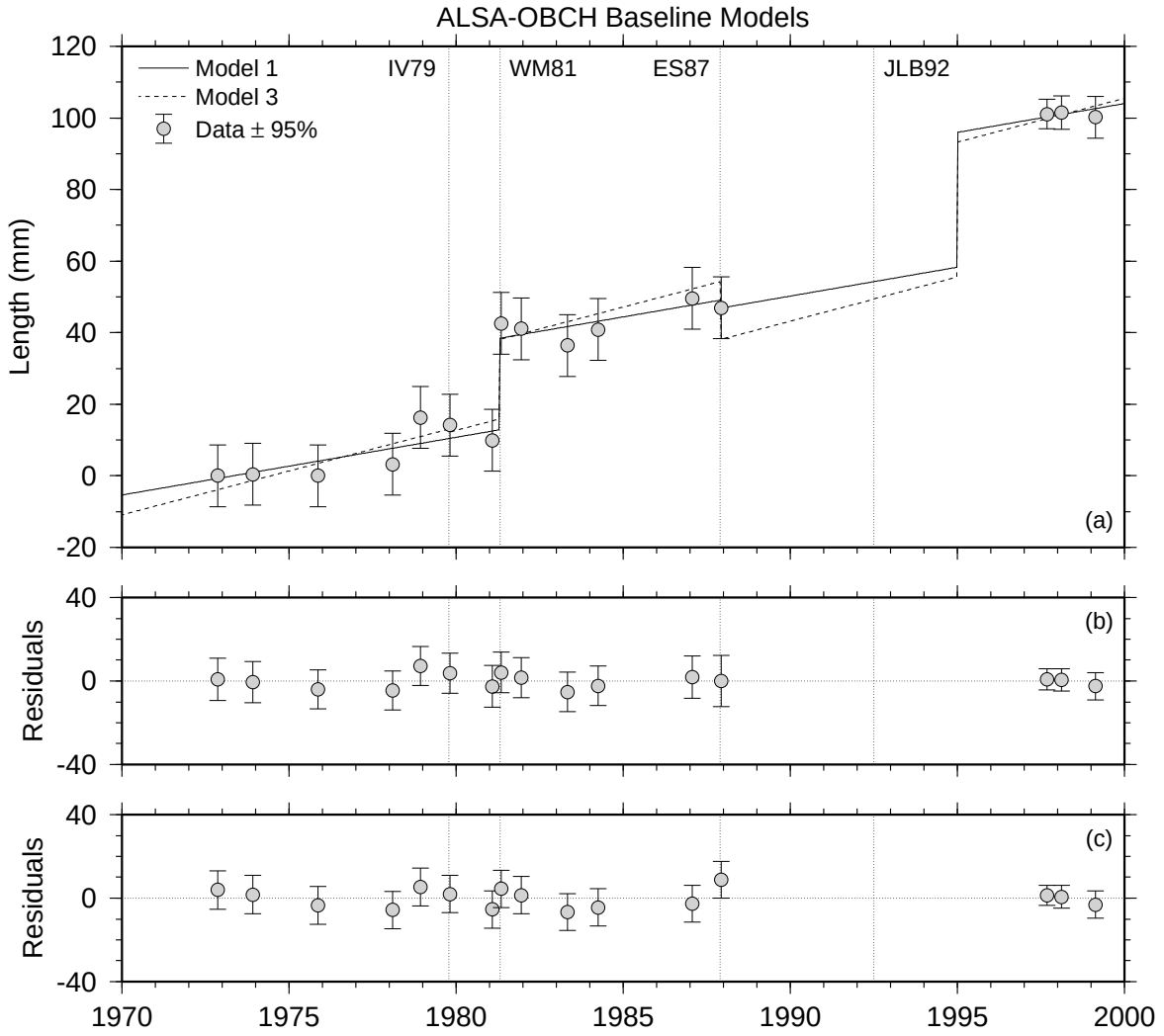

Figure 6. (a) Length time series and model fits for ALSA-OBCH baseline. Lines and circles are as in Figure 5. Note the additional offset at 1995.0 to account for anomalous motion of ALSA; in this case, the discrepancy between the expected value from trilateration and observed GPS measurement is 37.7 ± 6.8 mm. Note that, with the addition of this offset, Model 1 fits the data well, while Model 3 does not. (b–c) Residuals (in mm) for Models 1 and 3, as in Figure 5. Note that all residuals are compatible with zero misfit once the additional offset is added.

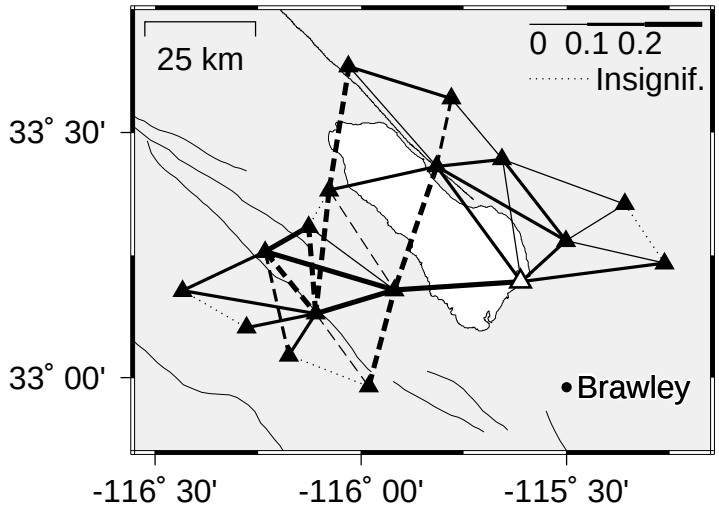

Figure 7. Baseline strain rates for Model 1. Baselines which are stretching are solid, while contracting lines are dashed; line thickness varies with strain rate as shown in upper right, with values in μstrain/yr. ALSA is marked by an empty triangle to emphasize that the ALSA baselines have an additional offset. Dotted lines represent baselines with insignificant (at 95% confidence) strain rates. Note expected pattern of N-S compression and E-W extension.

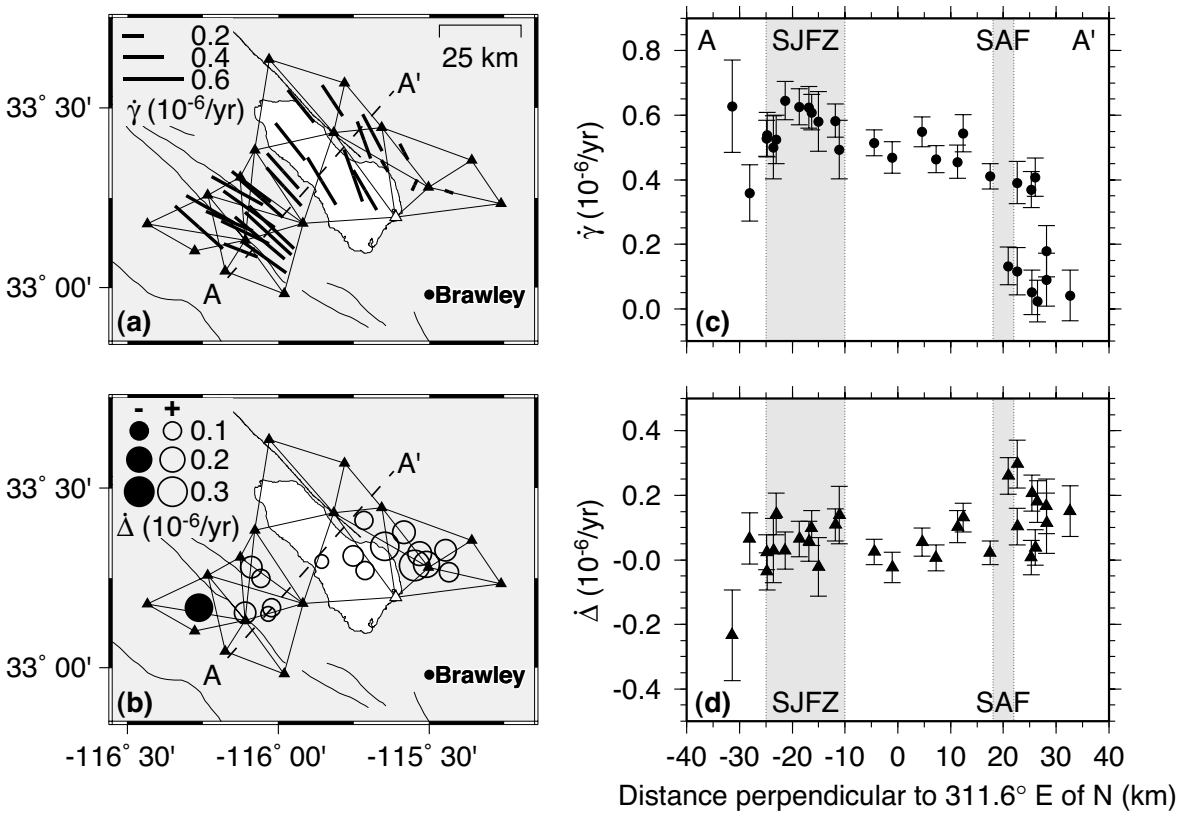

Figure 8. (a) $\dot{\gamma}$ and $\alpha_{\dot{\gamma}}$ for each unique four-station subnetwork, using the Model 1 principal strain rates. Bars are plotted at the centroid of each subnetwork with significant $\dot{\gamma}$, scale with $\dot{\gamma}$ as shown in the upper left, and are oriented parallel to $\alpha_{\dot{\gamma}}$. (b) $\dot{\Delta}$ for only those subnetworks with significant $\dot{\Delta}$. Open circles: $\dot{\Delta} > 0$; solid circles: $\dot{\Delta} < 0$. Circles scale with $\dot{\Delta}$ as shown in upper left. (c) Cross-network profile of $\dot{\gamma}$ (with 95% confidence regions) along the line A–A' in (a). Bands labeled "SJFZ" and "SAF" refer to the San Jacinto Fault Zone and San Andreas Fault, respectively. The SJFZ band is wider because the SJFZ has multiple fault strands through our network, while the SAF is relatively simple. (d) Profile of dilatation rates. Note high $\dot{\Delta}$ in southeastern part of network.

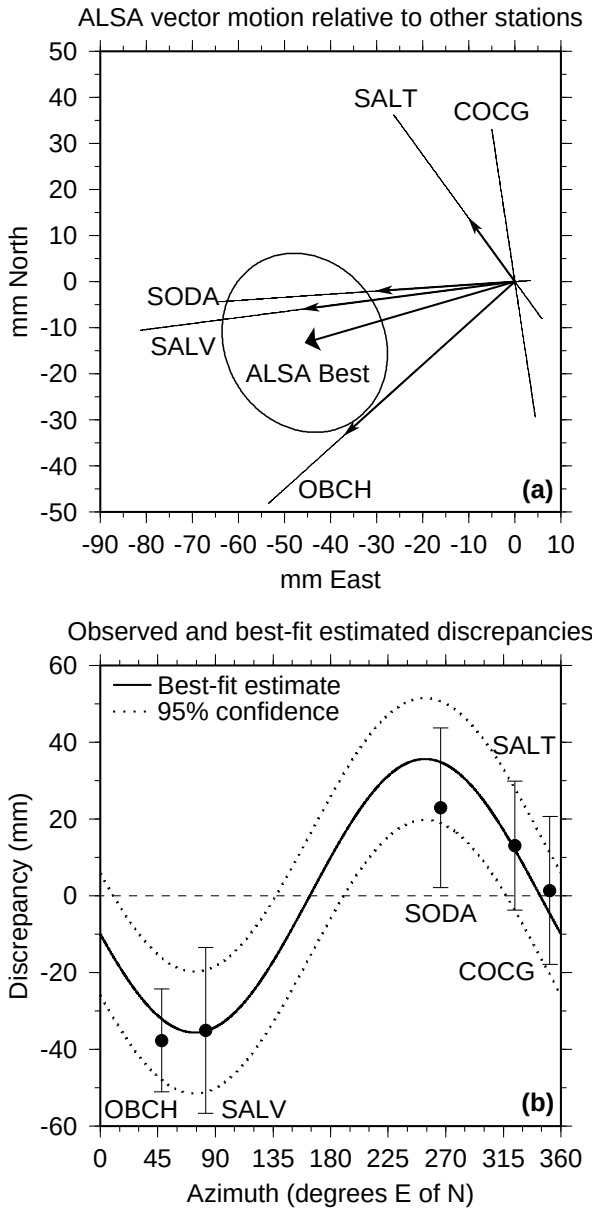

Figure B1. (a) Black vectors with thin arrowheads show the observed offsets in the ALSA baselines. Thin lines show 95% confidence limits on the observed offsets. Heavy arrow with wide head and 95% confidence limit shows best-fit motion of ALSA. (b) Solid line with dotted lines representing 95% confidence intervals shows baseline offsets expected due to ALSA best-fit motion. Circles with 95% confidence bars are observed offsets for Alamo baselines; these are fit well by the best-fit model.